Supporting Information

Nano-confinement effects on enhanced reversibility of redox reactions coupled with an irreversible chemical process by electrolysis acceleration in nanoporous carbon electrodes for redox-enhanced electrochemical capacitor

Jaehyun Jeon[†, ◊,‡], *Jihye Lee*[†,‡] *Kyu Yeon Jang*[◊,§] *Hana Yoon**[,◊], *and Jinho Chang**[,†]

[†]Department of Chemistry and Research Institute for Convergence of Basic Science, Hanyang University, 222 Wangsimni-ro, Seongdong-gu, Seoul 04763, Republic of Korea

[◊] Korea Institute of Energy Research (KIER), Daejeon 34129, Republic of Korea

[§] Department of Advanced Energy Technologies and System Engineering, Korea University of Science and Technology (UST), Daejeon 34113, Republic of Korea

[‡]J. Jeon and J. Lee contributed equally to this work.

*Jinho Chang: jhcechem@hanyang.ac.kr

*Hana Yoon: hanayoon@kier.re.kr

KEYWORDS: electrochemical capacitor, irreversible chemical reaction, enhanced reversibility, nanoporous carbon electrode, nanoconfinement effect

Contents

Calculation of the specific capacitance ·····S-5

Figure S1. ·····S-6

The chemical structures of hexahydroxybenzene (HHB), tetrahydroxy-1, 4-benzoquinone (THQ), rhodizonic acid (RDZ), rhodizonic acid dihydrate (RDZ·$2H_2O$), cyclohexanehexone (CHH), cyclohexanehexone dihydrate (CHH·$2H_2O$), cyclohexanehexone octahydrate (CHH·$8H_2O$).

Figure S2. ·····S-7

(a) Simulated CVs based on $E_1E_2C_1E_3C_2$, which are the same as shown in Figure 1e, and (b) dimensionless concentration profiles of all chemical species in the simulation as a function of the distance from an electrode surface at various values of *H*, which are designated on the CV of Figure S2a.

Figure S3. ·····S-8

2D axial symmetric domain of the simulation for electrolysis rate.

Figure S4. ·····S-9

FE-SEM images of (a) micro-C, (b) meso-C and (c) PG.

Figure S5. ·····S-10

The contact angles of a droplet composed of an aqueous electrolyte with 1 M H_2SO_4 on (a) micro- and (b) meso-C for the estimation of wettability.

Figure S6. ·····S-11

De-convoluted high-resolution C1s XPS spectra of (a) micro- and (b) meso-C.

Figure S7. ·····S-12

CVs exhibiting integrated areas for the estimation of Q_{red} and Q_{ox} in Figure 6.

Figure S8. ·····S-13

CVs measured in (a) 1M H_2SO_4 aqueous solutions with/without 5 mM HHB on PG electrode and (b) 1M H_2SO_4 aqueous solutions on HHB-absorbed PG electrode at 5 mV s^{-1}.

Figure S9. ·····S-14

Simulated *i-t* curves based on the EC scheme at the constantly applied potential, in which current is limited by mass transfer in micro- and meso-C with r_{pore} = 1.072 nm and 1.9 nm, with different kinetic parameters: (a) k_f = 1 and 5000 s^{-1} with constant k_b = 1 s^{-1}, (b) k_b = 0.1, 1, and 1.5 s^{-1} with constant k_f = 5000 s^{-1}; other parameters for the simulation are detailed in Table S2.

Figure S10. ·····S-15

The successive CV from HHB adsorbed micro-C electrode in either (a) a conventional three electrodes cell containing *ca.* 10 mL of an aqueous solution or (b) a compact cell composed of micro-C coated with HHB|1M H_2SO_4|micro-C.

Figure S11. ·····S-16

CVs measured in 1M H_2SO_4 aqueous solution on micro- and meso-C electrodes.

Figure S12. ·····S-17

The cell voltage vs. time for open-circuit (t_{oc}) after measured from the two asymmetric electrochemical cells composed of either micro- (black) or meso-C (red) after a constant 0.5 A g^{-1} was applied to render the cell voltage of 1 V during the charging process.

Figure S13. ·····S-18

Comparison of cycle stability of pristine cells and RDZ-coated asymmetric cells. Cycle stability tested at 0.1 V s^{-1}.

Table S1. ·····S-19

Reactions and corresponding parameters for the simulation shown in Figure 1.

Table S2. ·····S-20

Reactions and corresponding parameters for the simulation shown in Figure 2 and Figure S9.

References ····· S-21

Calculation of the specific gravimetric capacitance in electrochemical capacitors.

The specific gravimetric capacitance, $C_{spec,\,cell}$ (F g^{-1}) was calculated from the charge/discharge curve using Equation S1.[1,2]

$$\boldsymbol{C_{spec,cell} = i \cdot \Delta t/(\Delta E \cdot m)}, \qquad (1)$$

where ΔE is the voltage window, i is the charge/discharge current, and m is the mass of the active material; for the estimation of C_{spec} in the full cell.

Because the charges stored in each electrode are equal ($\boldsymbol{q_+ = q_-}$), the capacitance of each electrode was calculated by Equations S2 and S3.[3]

$$\boldsymbol{C_+ \Delta V_+ = C_- \Delta V_-} \qquad (2)$$

$$\boldsymbol{\frac{1}{C_{cell}} = \frac{1}{C_+} + \frac{1}{C_-}} \qquad (3)$$

C_{spec} from the stability test in Figure S13 performed by cyclic voltammetry at 0.1 V s^{-1} was estimated by Equation S4.[4,5]

$$\boldsymbol{C_{spec,cell} = \frac{\frac{\int i dV}{\Delta E v}}{m}}, \qquad (4)$$

where v is the scan rate.

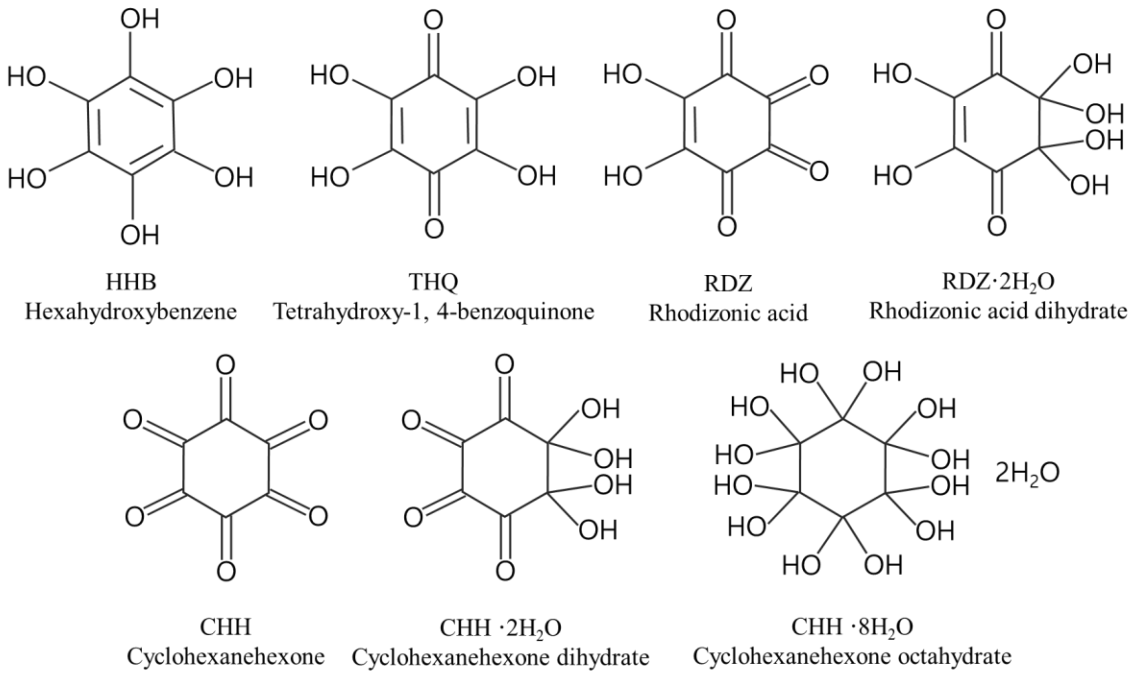

Figure S1. Chemical structures of hexahydroxybenzene (HHB), tetrahydroxy-1, 4-benzoquinone (THQ), rhodizonic acid (RDZ), rhodizonic acid dihydrate (RDZ·$2H_2O$), cyclohexanehexone (CHH), cyclohexanehexone dihydrate (CHH·$2H_2O$), cyclohexanehexone octahydrate (CHH·$8H_2O$).

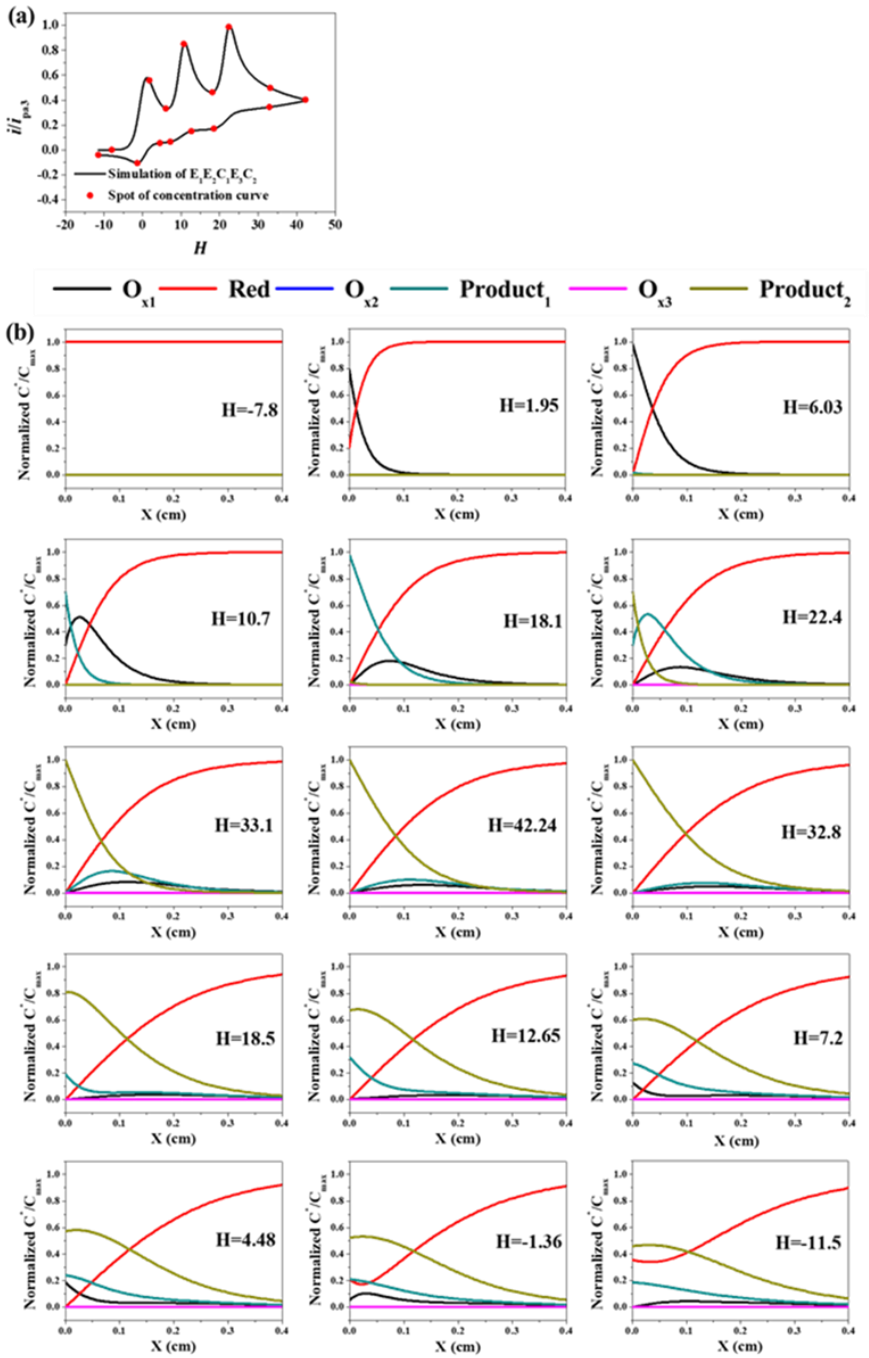

Figure S2. (a) Simulated CVs based on $E_1E_2C_1E_3C_2$, which are the same as shown in Figure 1e, and (b) dimensionless concentration profiles of all chemical species in the simulation as a function of the distance from an electrode surface at various values of *H*, which are designated on the CV of Figure S2a.

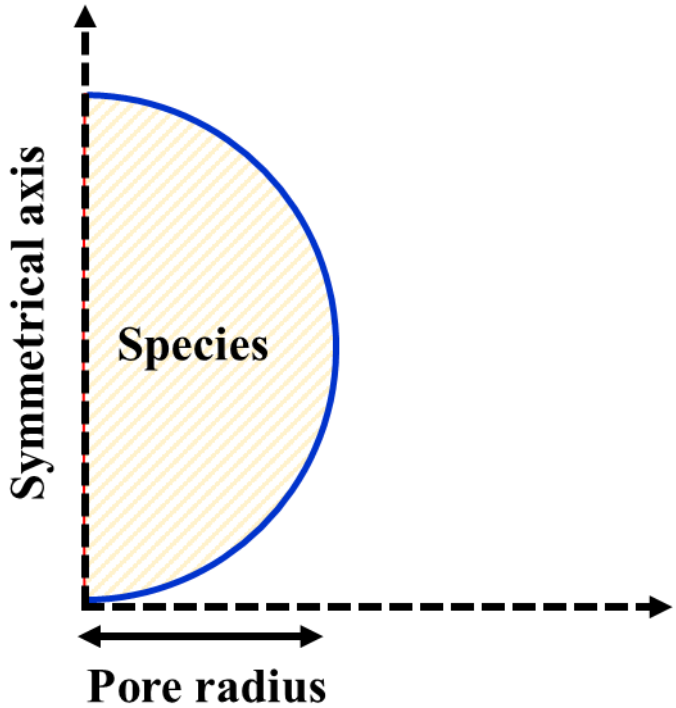

Figure S3. 2D axial symmetric domain of the simulation for electrolysis rate.

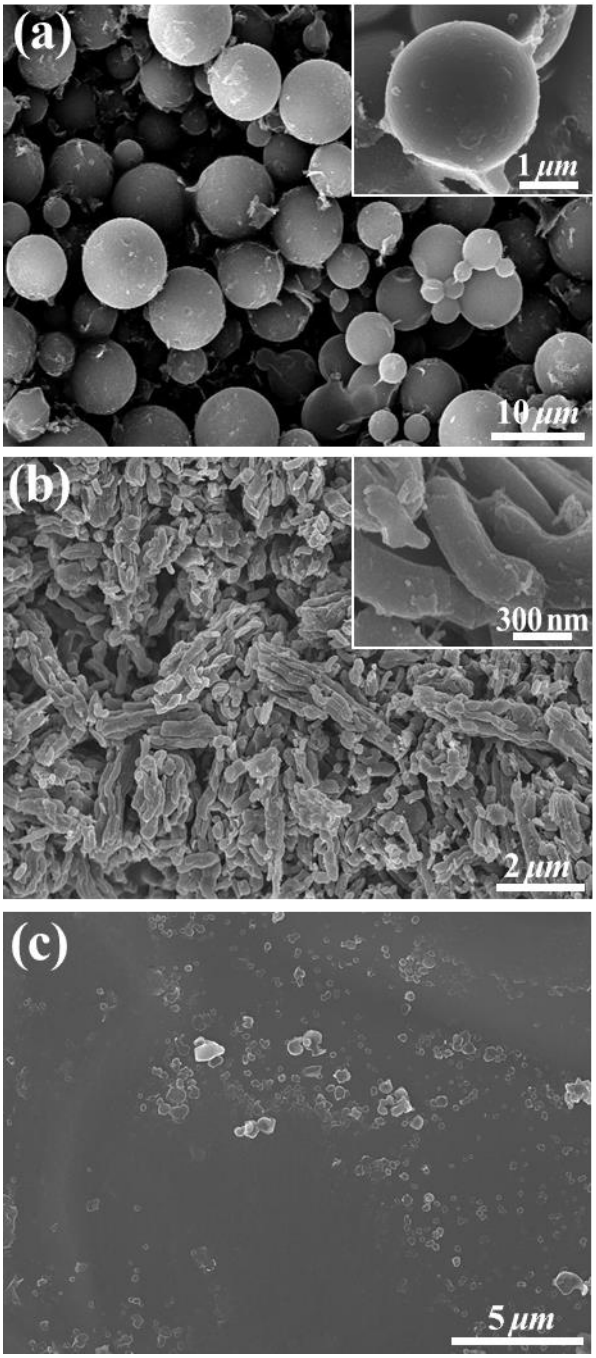

Figure S4. FE-SEM images of (a) micro-C, (b) meso-C and (c) PG.

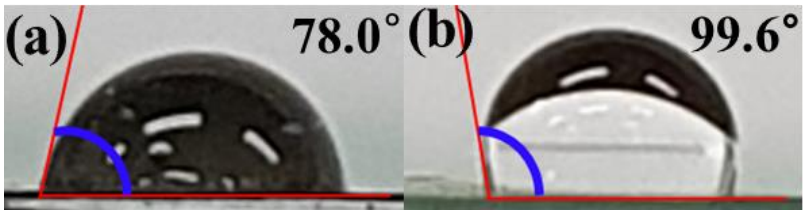

Figure S5. The contact angles of a droplet composed of an aqueous electrolyte with 1 M H_2SO_4 on (a) micro- and (b) meso-C for the estimation of wettability.

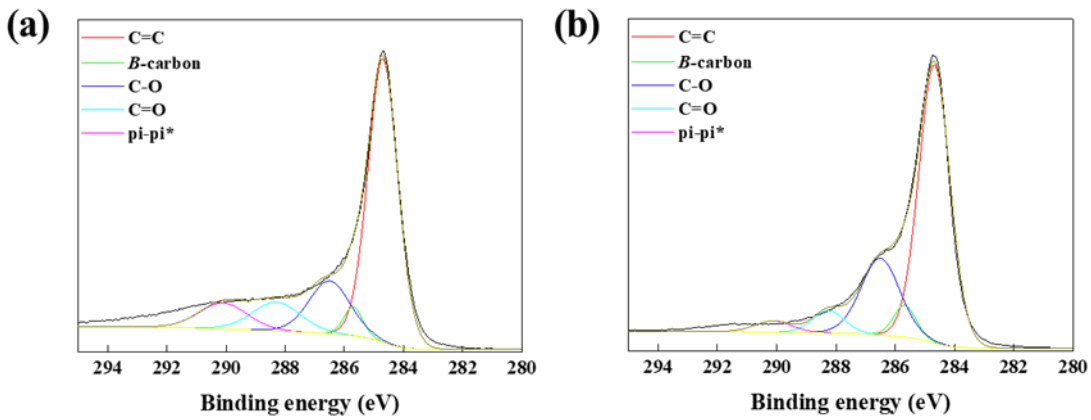

Figure S6. De-convoluted high-resolution C1s XPS spectra of (a) micro- and (b) meso-C. The C 1s spectrum of carbon powder exhibited a main peak at 284.7 eV, which is attributed to sp^2 C-C bonds in a graphite carbon.[6] In addition, characteristic peaks at 285.7 eV, 286.5 eV, 288.3 eV, and 290.1 eV represent β-carbon,[7] C-O,[8] C=O,[9] and π-π*,[10] respectively.

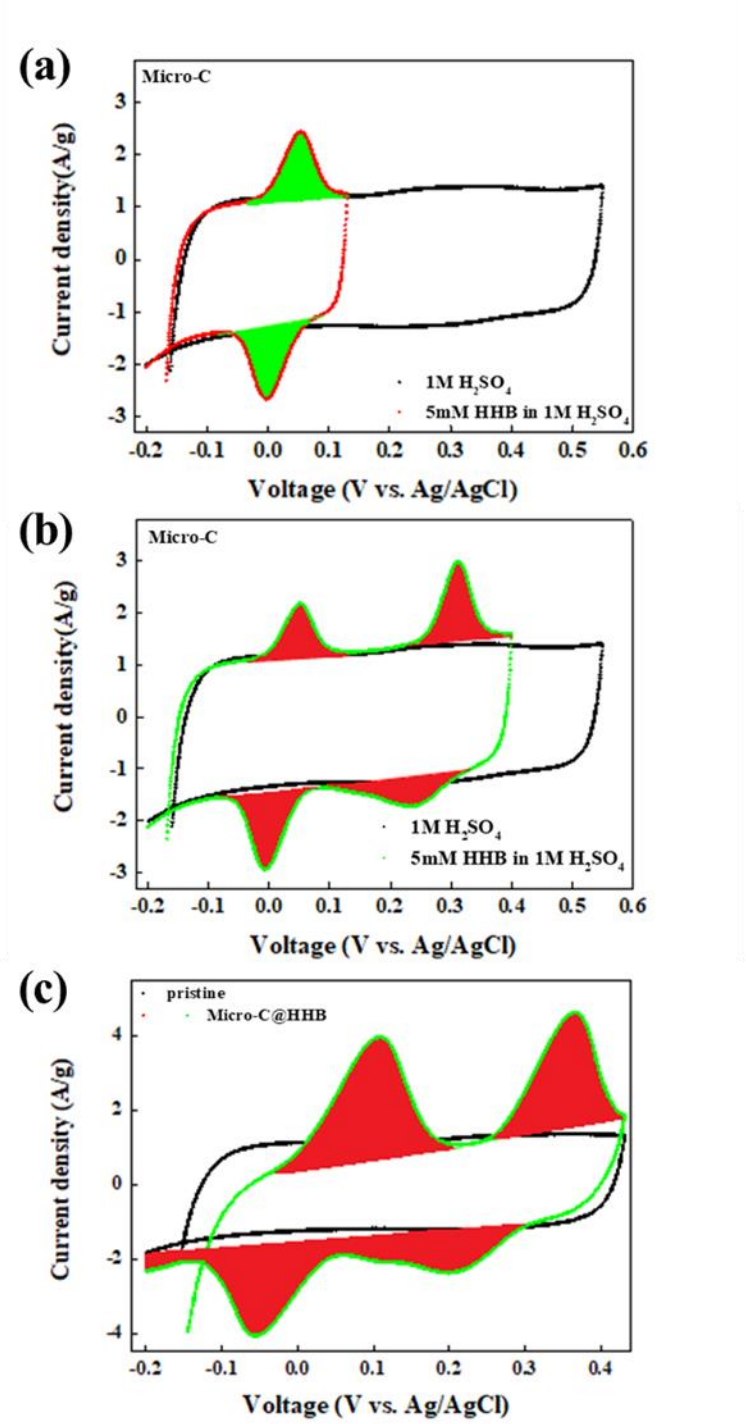

Figure S7. CVs exhibiting integrated areas for the estimation of Q_{red} and Q_{ox} in Figure 6.

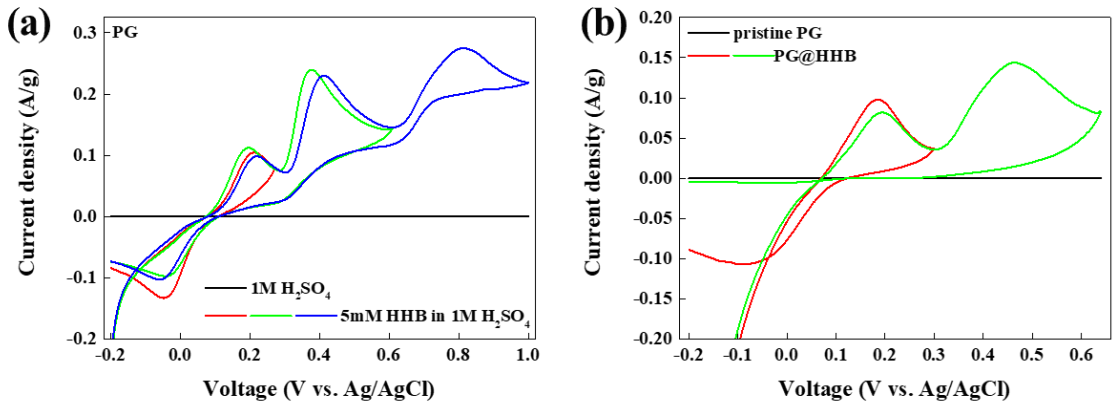

Figure S8. CVs measured in (a) 1M H_2SO_4 aqueous solutions with/without 5 mM HHB on PG electrode and (b) 1M H_2SO_4 aqueous solutions on HHB-absorbed PG electrode at 5 mV s^{-1}.

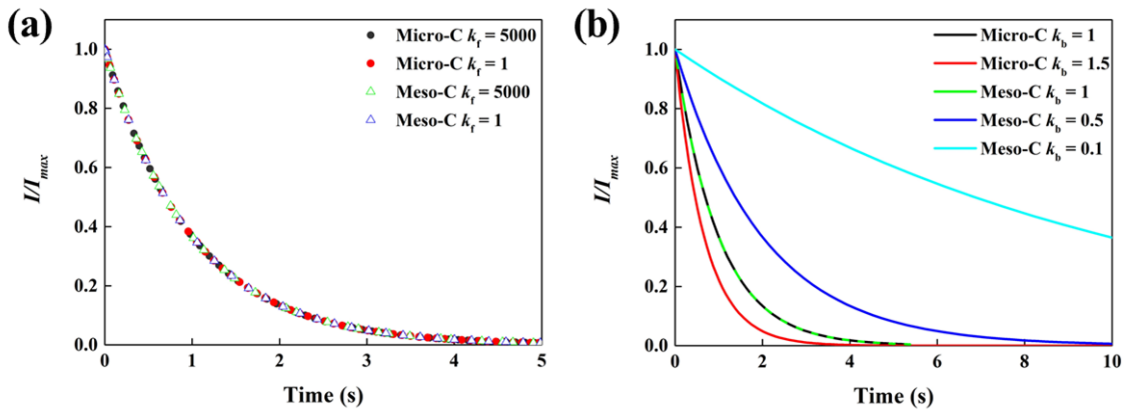

Figure S9. Simulated *i-t* curves based on the EC scheme at the constantly applied potential, in which current is limited by mass transfer in micro- and meso-C with r_{pore} = 1.072 nm and 1.9 nm, with different kinetic parameters: (a) k_f = 1 and 5000 s^{-1} with constant k_b = 1 s^{-1}, (b) k_b = 0.1, 1, and 1.5 s^{-1} with constant k_f = 5000 s^{-1}; other parameters for the simulation are detailed in Table S2.

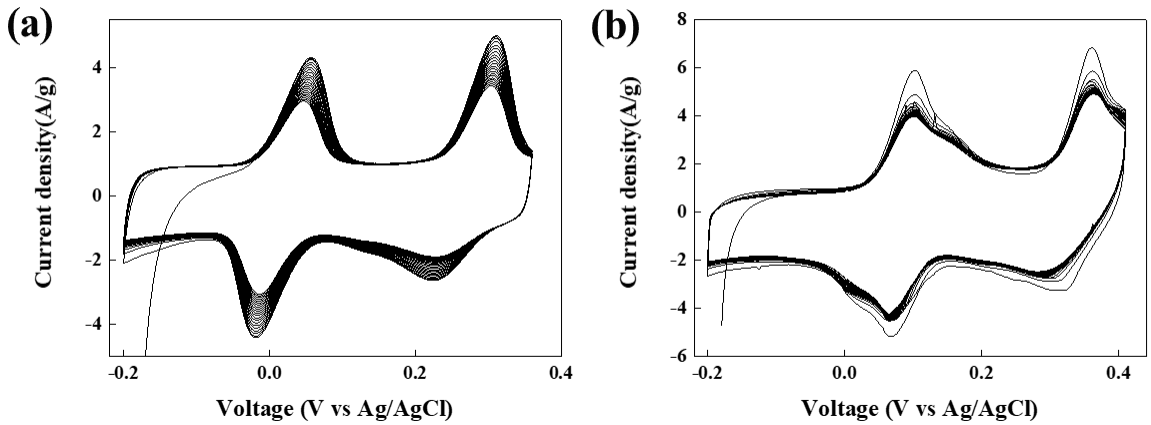

Figure S10. The successive CV from HHB adsorbed micro-C electrode in either (a) a conventional three electrodes cell containing *ca.* 10 mL of an aqueous solution or (b) a compact cell composed of micro-C coated with HHB|1M H_2SO_4|micro-C.

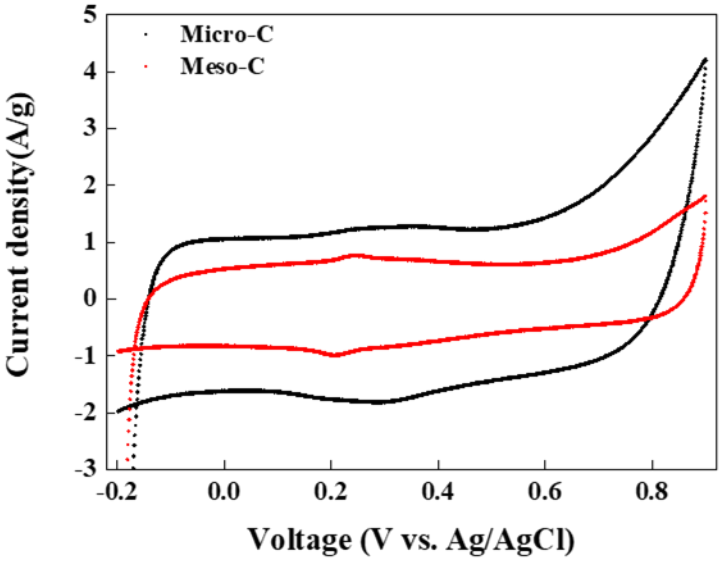

Figure S11. CVs measured in 1M H_2SO_4 aqueous solution on micro- and meso-C electrodes.

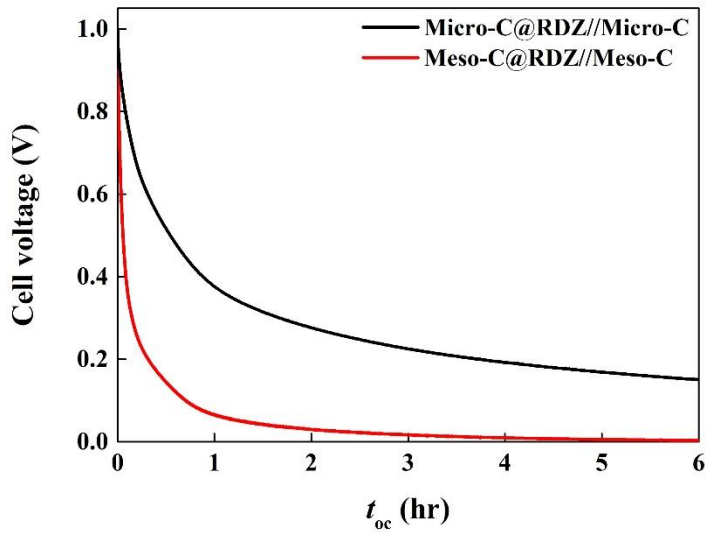

Figure S12. The cell voltage vs. time for open-circuit (t_{oc}) after measured from the two asymmetric electrochemical cells composed of either micro- (black) or meso-C (red) after a constant 0.5 A g^{-1} was applied to render the cell voltage of 1 V during the charging process.

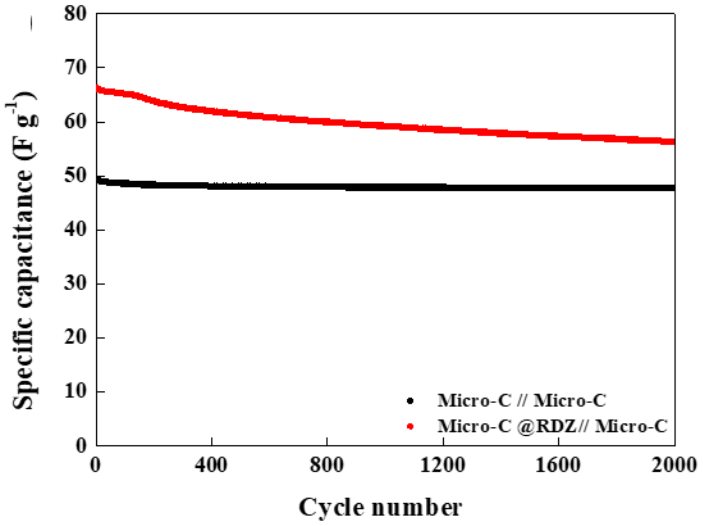

Figure S13. Comparison of cycle stability of pristine cells and RDZ-coated asymmetric cells. Cycle stability tested at 0.1 V s^{-1}.

Table S1. Reactions and corresponding parameters for the simulation shown in Figure 1.

Charge transfer reaction			
	E^0 (V)		k_s (cm/s)
$Ox_1 + e^- \rightleftharpoons Red$	0.1		1
$Ox_2 + e^- \rightleftharpoons Ox_1$	0.5		1
$Ox_3 + e^- \rightleftharpoons Product_1$	0.8		1
Chemical reaction			
	K_{eq}		k_f (s^{-1})
$Ox_2 \rightleftharpoons Product_1$	10000		10000
$Ox_3 \rightleftharpoons Product_2$	10000		10000
Concentration			
Species	D (cm^2/s)	C_{anal} (mol/L)	C_{ini} (mol/L)
$\boldsymbol{C_{Red}}$	5×10^{-5}	0.005	0.005
$\boldsymbol{C_{O_{x1}}}$	5×10^{-5}	0	0
$\boldsymbol{C_{O_{x2}}}$	5×10^{-5}	0	0
$\boldsymbol{C_{Product_1}}$	5×10^{-5}	0	0
$\boldsymbol{C_{O_{x3}}}$	5×10^{-5}	0	0
$\boldsymbol{C_{Product_2}}$	5×10^{-5}	0	0

Table S2. Reactions and corresponding parameters for the simulation shown in Figure 2 and Figure S9.

Reactions	Parameters			
	k^0	E_{eq}	α	Applied potential
$B + e^- \rightleftharpoons A$	0.1 cm/s	0.4 V	0.5	0 V
$B \rightleftharpoons C$	r_{pore}, k_f, k_b (s^{-1}) = variable			
Relevant time-dependent diffusion equations				
(1) $\frac{\partial C_A}{\partial t} = D_A \left[\frac{\partial^2 C_A}{\partial r^2} + \frac{2}{r}\frac{\partial C_A}{\partial r}\right]$				
(2) $\frac{\partial C_B}{\partial t} = D_B \left[\frac{\partial^2 C_B}{\partial r^2} + \frac{2}{r}\frac{\partial C_B}{\partial r}\right] - k_f C_B + k_b C_C$				
(3) $\frac{\partial C_C}{\partial t} = D_B \left[\frac{\partial^2 C_C}{\partial r^2} + \frac{2}{r}\frac{\partial C_C}{\partial r}\right] + k_f C_B - k_b C_C$				
Initial condition, completing the definition of the problem				
t = 0, $C_A = C_B = 0$ mM $C_C = 5$mM				
$D_A = D_B = D_C = 5 \times 10^{-6}$ cm^2/s				

References

(1) Wang, H.; Yi, H.; Zhu, C.; Wang, X.; Jin Fan, H. Functionalized highly porous graphitic carbon fibers for high-rate supercapacitive electrodes. *Nano Energy* **2015,** *13*, 658-669.

(2) Guo, B.; Yang, Y.; Hu, Z.; An, Y.; Zhang, Q.; Yang, X.; Wang, X.; Wu, H. Redox-active organic molecules functionalized nitrogen-doped porous carbon derived from metal-organic framework as electrode materials for supercapacitor. *Electrochim. Acta* **2017,** *223*, 74-84.

(3) Roldán, S.; Granda, M.; Menéndez, R.; Santamaría, R.; Blanco, C. Mechanisms of Energy Storage in Carbon-Based Supercapacitors Modified with a Quinoid Redox-Active Electrolyte. *J. Phys. Chem. C* **2011,** *115* (35), 17606-17611.

(4) Warren, R.; Sammoura, F.; Tounsi, F.; Sanghadasa, M.; Lin, L. Highly active ruthenium oxide coating via ALD and electrochemical activation in supercapacitor applications. *J. Mater. Chem. A* **2015,** *3* (30), 15568-15575.

(5) Sheng, L.; Jiang, L.; Wei, T.; Liu, Z.; Fan, Z. Spatial Charge Storage within Honeycomb-Carbon Frameworks for Ultrafast Supercapacitors with High Energy and Power Densities. *Adv. Energy Mater.* **2017,** *7* (19), 1700668.

(6) Sheng, Z.-H.; Zheng, X.-Q.; Xu, J.-Y.; Bao, W.-J.; Wang, F.-B.; Xia, X.-H. Electrochemical sensor based on nitrogen doped graphene: Simultaneous determination of ascorbic acid, dopamine and uric acid. *Biosens. Bioelectron.* **2012,** *34* (1), 125-131.

(7) Le Comte, A.; Chhin, D.; Gagnon, A.; Retoux, R.; Brousse, T.; Bélanger, D. Spontaneous grafting of 9,10-phenanthrenequinone on porous carbon as an active electrode material in an electrochemical capacitor in an alkaline electrolyte. *J. Mater. Chem. A* **2015,** *3* (11), 6146-6156.

(8) Yen, M.-Y.; Teng, C.-C.; Hsiao, M.-C.; Liu, P.-I.; Chuang, W.-P.; Ma, C.-C. M.; Hsieh, C.-K.; Tsai, M.-C.; Tsai, C.-H. Platinum nanoparticles/graphene composite catalyst as a novel composite

counter electrode for high performance dye-sensitized solar cells. *J. Mater. Chem.* **2011,** *21 (34)*, 12880-12888.

(9) Lin, Z.-Q.; Xie, J.; Zhang, B.-W.; Li, J.-W.; Weng, J.; Song, R.-B.; Huang, X.; Zhang, H.; Li, H.; Liu, Y.; Xu, Z. J.; Huang, W.; Zhang, Q. Solution-processed nitrogen-rich graphene-like holey conjugated polymer for efficient lithium ion storage. *Nano Energy* **2017,** *41*, 117-127.

(10) Puziy, A. M.; Poddubnaya, O. I.; Socha, R. P.; Gurgul, J.; Wisniewski, M. XPS and NMR studies of phosphoric acid activated carbons. *Carbon* **2008,** *46* (15), 2113-2123.